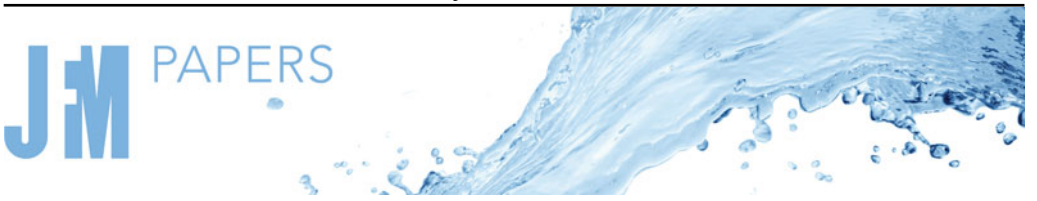
J. Fluid Mech. (2025), *vol.* 1014, A4, doi:10.1017/jfm.2025.10281



Modulation of the instability growth at sequential heavy–light interfaces in a shocked dual layer

Chenren Chen[1], **Xuan Li**[1], **Yifan Ma**[1], **Zhigang Zhai**[1] **and Xisheng Luo**[1,2]

[1]Advanced Propulsion Laboratory, Department of Modern Mechanics, University of Science and Technology of China, Hefei 230026, PR China

[2]State Key Laboratory of High-Temperature Gas Dynamics, Institute of Mechanics, Chinese Academy of Sciences, Beijing 100190, PR China

Corresponding authors: Xisheng Luo, xluo@ustc.edu.cn; Zhigang Zhai, sanjing@ustc.edu.cn

(Received 21 March 2025; revised 9 May 2025; accepted 20 May 2025)

We present a theoretical framework and validation for manipulating instability growth in shock-accelerated dual-layer material systems, which feature a light–heavy interface followed by two sequential heavy–light interfaces. An analytical model is first developed to predict perturbation evolution at the two heavy–light interfaces, explicitly incorporating the effects of reverberating waves within the dual-layer structure. The model identifies five distinct control regimes for instability modulation. Shock-tube experiments and numerical simulations are designed to validate these regimes, successfully realising all five predicted states. Notably, the selective growth stagnation of a perturbation at either the upstream or downstream heavy–light interface is realised numerically by tuning the initial separation distances of the three interfaces. This work elucidates the critical role of the wave dynamics in governing interface evolution of a shocked dual layer, offering insights for mitigating hydrodynamic instabilities in practical scenarios such as inertial confinement fusion.

Key words: shock waves

1. Introduction

The Richtmyer–Meshkov instability (RMI), triggered by shock acceleration at perturbed material interfaces, arises from baroclinic vorticity generated by misaligned pressure and density gradients (Richtmyer 1960; Meshkov 1969). This instability governs fluid mixing in systems ranging from astrophysical phenomena like supernova remnants (Kuranz, Park & Huntington 2018) to engineering applications such as scramjet combustion (Urzay 2018) and inertial confinement fusion (ICF) (Kritcher *et al.* 2022; Zylstra *et al.* 2022), and

© The Author(s), 2025. Published by Cambridge University Press.

https://doi.org/10.1017/jfm.2025.10281 Published online by Cambridge University Press

several reviews have concluded the progress of the RMI development (Brouillette 2002; Ranjan, Oakley & Bonazza 2011; Zhou 2017*a*,*b*; Zhou *et al.* 2021, 2025). While RMI enhancement is critical for fuel–air mixing in propulsion systems, its suppression remains imperative for improving the efficiency of ICF, where interfacial mixing degrades hot-spot compression (Spears *et al.* 2014; Betti & Hurricane 2016).

For a single-shocked interface, the perturbation evolution depends on interface type: light–heavy interfaces (the shock passes through the interface from a light fluid to a heavy fluid) exhibit sustained amplitude growth after shock compression (Richtmyer 1960), whereas heavy–light interfaces (the shock passes through the interface from a heavy fluid to a light fluid) undergo phase inversion prior to growth. In both cases, intrinsic instability progression remains challenging to suppress. Vorticity dynamics dominates the behaviour of post-shock interface perturbation, motivating strategies to modulate RMI through second wave impacts that alter vorticity deposition. Mikaelian (1985) pioneered this approach, demonstrating that a second shock impact could classify RMI evolution into thirteen distinct regimes. Among these regimes, growth stagnation, the complete cessation of amplitude development, represents a promising pathway for controlling interfacial mixing in shock-driven systems.

In previous work, second wave impacts have proven effective in suppressing RMI growth at single interfaces. For light–heavy configurations with single-mode perturbations, growth stagnation has been achieved through appropriate reflected shocks in both numerical studies (Mikaelian 2010) and shock-tube experiments (Chen *et al.* 2023*b*). Conversely, stabilising RMI at heavy–light interfaces requires successive same-direction shocks, which has been validated through numerical simulations (Charakhch'yan 2000, 2001), and recent high-energy density physics experiments (Merritt *et al.* 2023; Schill, Armstrong & Nguyen 2024) and shock-tube experiments (Zhai *et al.* 2025). Notably, reflected rarefaction waves offer an alternative control strategy by imparting accelerations aligned with the initial shock direction, enabling suppression of heavy–light interface perturbations in shock-tube systems (Chen *et al.* 2023*a*). These results collectively establish second wave interactions as a robust methodology for single-interface RMI modulation.

In real-world scenarios, RMI typically occurs in multi-interface systems, and prior research has focused on a single fluid layer bounded by two interfaces, typically generated via the gas curtain technique (Jacobs *et al.* 1993), the soap-film technique (Liang & Luo 2023*b*) or the oscillating technique (Schalles *et al.* 2024). Unlike single interfaces, a shocked fluid layer exhibits a unique dynamics due to wave reverberation and interface coupling. Theoretical frameworks have quantified how these coupled phenomena govern layer evolution (Mikaelian 1985; Jacobs *et al.* 1995; Chen *et al.* 2024*b*). In numerical simulations, the phase effect (Liang 2022), nonlinear effect (Chen *et al.* 2024*a*) and geometric configuration effect (West *et al.* 2024) on the RMI growth of a fluid layer have recently been investigated. Efforts to control the RMI growth of a layer have achieved partial success. Mikaelian (1996) numerically demonstrated growth stagnation at the upstream interface of a heavy layer, while recent works attenuated downstream interface perturbations through upstream interface shape optimisation and layer-width adjustment (Sterbentz *et al.* 2022; Chen *et al.* 2024*b*). Numerical simulations also suggested selective growth stagnation at either the upstream or downstream interface in a heavy layer (Cong *et al.* 2024) and sequential heavy–light interface configurations (Liang & Luo 2023*a*). Recently, Mikaelian (2025) theoretically proposed quantitative approaches that suppress the RMI at a layer through the interface-coupling effect. However, these strategies necessitate stringent initial conditions such as specific amplitude ratios, severely constraining their practical utility in real-world systems.

https://doi.org/10.1017/jfm.2025.10281 Published online by Cambridge University Press

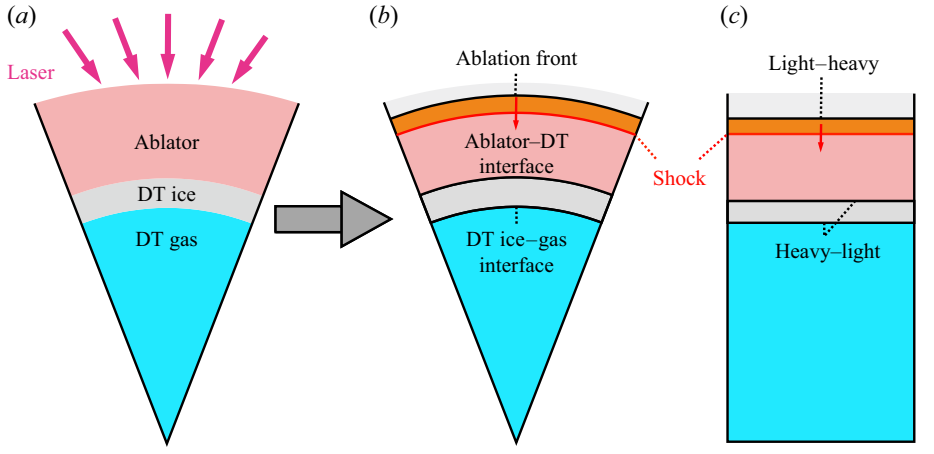


Figure 1. Schematic diagrams of the classical ICF target consisting of ablator, DT ice fuel and DT gas fuel (*a*) before the ignition, (*b*) during the ignition and (*c*) the dual-layer system considered in this work.

In ICF, capsules, laser-driven shocks, induce perturbation growth at three critical interfaces: the ablation front (light–heavy interface) (Qiao & Lan 2021), the interface between ablator and deuterium–tritium (DT) ice (heavy–light interface) (Amendt 2021) and the DT ice–gas fuel interface (heavy–light interface) (Lobatchev & Betti 2000), as shown in figures 1(*a*)–1(*b*). These interfaces collectively form a dual-layer structure, comprising one light–heavy and two sequential heavy–light interfaces. The evolution of the shocked dual layer exhibits significantly greater complexity than single-layer systems, with existing studies remaining limited in scope. While prior work has quantified the interface-coupling effects for a dual layer in both linear (Liang & Luo 2021) and nonlinear regimes (Liu *et al.* 2018*b*), these analyses assumed idealised vacuum conditions, neglecting external fluid interactions with the layer. Crucially, the coupled dynamics of wave reverberation and interface coupling in a dual-layer system remains uncharacterised, particularly for systems with realistic boundary constraints. This knowledge gap obstructs the development of predictive control frameworks, motivating the present study.

This work addresses gaps by investigating a shock-accelerated dual-layer system comprising a flat light–heavy interface followed by two heavy–light interfaces, as shown in figure 1(*c*), designed to emulate RMI at the three classical interfaces of an ICF capsule. Recognising the dominant role of the inner DT ice–gas interface roughness in ignition performance (Bodner *et al.* 1998), we construct a prototypical dual-layer system with a flat light–heavy interface, an unperturbed upstream heavy–light interface and a single-mode downstream heavy–light interface. A theoretical framework is developed to resolve both the effects of wave reverberation and interface coupling on perturbation growth at the heavy–light interfaces. According to the model, the possibilities of the perturbation growth at the two heavy–light interfaces are analysed, and then shock-tube experiments and numerical simulations are conducted for validation.

2. Theoretical analysis

2.1. *Derivation of the model*

Dual-layer systems exhibit substantially enhanced complexity in wave–interface interactions compared with single-layer configurations, with the interplay of the coupled interface dynamics and reverberating waves posing substantial challenges for quantitative

https://doi.org/10.1017/jfm.2025.10281 Published online by Cambridge University Press

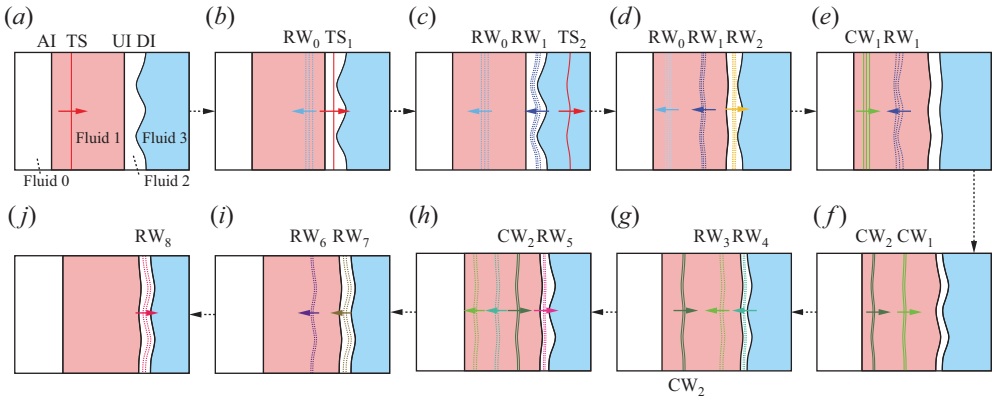


Figure 2. Schematic diagrams of a shock accelerating a fluid dual-layer which contains a AI and two successive heavy-light interfaces. (*a*) The incident shock has passed through the first AI, generating the transmitted shock (TS), which is about to impact the upstream UI; (*b*) the rarefaction waves (RW_0) moving towards AI are generated by TS interacting with UI and the second transmitted shock (TS_1) moves to DI; (*c*) after TS_1 passes through DI, the third transmitted shock (TS_2) is generated and the rarefaction waves RW_1 moving to UI are reflected; (*d*) after the RW_1 pass through UI, rarefaction waves RW_2 are reflected to move to DI and the RW_1 move to AI following RW_0; (*e*) RW_0 has struck AI, the reflected compression waves CW_1 are formed, while the RW_1 have not reached AI and are about to collide with CW_1; (*f*) after the RW_1 interact with AI, the compression waves CW_2 are generated and move to UI following CW_1; (*g*) the CW_1, respectively, accelerate UI and DI, which create rarefaction waves RW_3 and RW_4 from UI and DI; (*h*) the RW_4 interact with UI, forming the RW_5 moving downwards, and the CW_2 is about to impact UI; (*i*) and (*j*) rarefaction waves RW_6 (RW_7) are generated by CW_2 impacting UI (DI) and rarefaction waves RW_8 are reflected by the interaction between RW_7 and UI. The left-most white area is the region of fluid 0, the pink area between AI and UI represents the region of heaviest fluid 1, the white area sandwiched between UI and DI is the region of fluid 2 with the medium density and the right-most blue area is the region of fluid 3 with the lowest density.

analysis (Mikaelian 1985). To isolate these effects, our model simplifies the system by maintaining flat geometries for both the light–heavy interface (AI) which is the first shock-impacted interface, and the upstream heavy–light interface (UI). This geometric design choice effectively suppresses perturbation growth at AI while eliminating its interaction with UI, thereby allowing focused analysis on the UI and downstream heavy-light interface (DI). Despite these simplifications, the presence of AI introduces additional wave-reverberation pathways within the dual-layer structure. Consequently, the perturbation evolution at DI remains inherently more complex relative to single-layer systems, as reverberation waves from AI persistently modulate the vorticity distribution at the interface. This controlled reduction of variables provides a foundational framework for resolving dual-layer instability mechanisms while preserving key physical drivers of multi-interface coupling.

As shown in figure 2(*a*), the stratified configuration comprises four distinct fluid domains: the first white area at the upstream side of AI is fluid 0 region, the pink area between AI and UI represents the region of fluid 1 with the highest density, the white area sandwiched between UI and DI is the region of fluid 2 with the medium density and the right-most blue area is the region of fluid 3 with the lowest density. In the present work, the fluid 1 is SF_6, both the fluids 0 and 2 are air and the fluid 3 is helium. We define L_0 and W_0 as the initial distance between UI and AI, i.e. the width of the pink SF_6 region (fluid 1 region), and the initial distance between UI and DI, i.e. the width of the second white region (fluid 2 region) sandwiched between SF_6 and helium, respectively. After the shock interacts with the dual layer (the shock passing through AI is defined as the transmitted shock, TS, here), the flat AI and TS move to UI and DI, as presented in

https://doi.org/10.1017/jfm.2025.10281 Published online by Cambridge University Press

figure 2(*a*). In figure 2(*b*), the unperturbed rarefaction waves (RW_0) and the second flat transmitted shock (TS_1) are generated after TS interacts with UI. In this work, the initial time is defined as the moment when TS_1 impacts DI. Following the interaction of TS_1 with DI, the perturbed rarefaction waves (RW_1) and the third transmitted shock (TS_2) are formed, as shown in figure 2(*c*). After the RW_1 pass through the unperturbed UI, UI is stretched and reflected rarefaction waves (RW_2) are generated and travel to DI, as shown in figure 2(*d*). During the wave–interface interactions, the amplitudes of the waves and interfaces will be altered, as described in detail in Appendix A.

After the RW_1 leave UI and RW_2 pass through DI, interface coupling begins to affect UI and DI, respectively. To quantify the interface coupling between UI and DI, the LL-model proposed by Liang & Luo (2022) is modified based on the different accelerations of UI and DI, and can be expressed as

$$\begin{aligned}&\dot{a}_{11}[\rho_1+\rho_2\tanh(kW/2)]+\dot{a}_{21}[\rho_3+\rho_2\tanh(kW/2)]\\&\quad=k(\rho_2-\rho_1)(a_{1+}\Delta u_1+a_{1R}^{+}\Delta u_{R1})+k(\rho_3-\rho_2)(a_{20}\Delta u_2+a_{2R}^{+}\Delta u_{R2}),\end{aligned}\tag{2.1}$$

$$\begin{aligned}&\dot{a}_{11}[\rho_1+\rho_2\coth(kW/2)]-\dot{a}_{21}[\rho_3+\rho_2\coth(kW/2)]\\&\quad=k(\rho_2-\rho_1)(a_{1+}\Delta u_1+a_{1R}^{+}\Delta u_{R1})-k(\rho_3-\rho_2)(a_{20}\Delta u_2+a_{2R}^{+}\Delta u_{R2}).\end{aligned}\tag{2.2}$$

Here, $\dot{a}_{11}$ is the amplitude growth of UI after the RW_1 acceleration and $\dot{a}_{21}$ is the amplitude growth of DI after the RW_2 acceleration; k is the perturbation wavenumber; a_{1+} is the amplitude of UI just after being impacted by TS and a_{20} is the average amplitude of the shocked and unshocked DI; a_{1R}^{+} and a_{2R}^{+} are the amplitudes of UI just being accelerated by the RW_1 and of DI just being impacted by the RW_2, respectively; ρ_1, ρ_2 and ρ_3 are the densities of fluid 1, fluid 2 and fluid 3, respectively, after the interaction of the RW_2 with DI; W is the distance between UI and DI after TS_1 collides with DI; Δu_1 (Δu_{R1}) is the jump velocity of UI induced by TS (RW_1); and Δu_2 (Δu_{R2}) is the jump velocity of DI induced by TS_1 (RW_2). The derivations of the modified LL-model and the related parameters are provided in Appendix A. According to (2.1)–(2.2), $\dot{a}_{11}$ and $\dot{a}_{21}$ can be predicted until other reverberating waves inside the dual layer affect the perturbation growth. Notably, the modified LL-model, which considers a three-fluid system, is employed to evaluate the interface coupling between UI and DI. In this work, the first shock-impacted AI and UI are initialised as flat, and a sufficiently large separation distance is imposed between AI and UI. This geometric configuration suppresses perturbation growth at AI and decouples AI–UI interactions, thereby isolating the interface-coupling mechanism between UI and DI. By eliminating extraneous dynamics, the study focuses exclusively on UI–DI coupling.

Due to the presence of AI, the compression waves CW_1 and CW_2 are generated, respectively, after the RW_0 and RW_1 interact with AI, and move successively towards UI, as shown in figures 2(*e*)–2(*f*). After the CW_1 accelerate UI and DI, the rarefaction waves RW_3 (RW_4) moving upstream are generated in fluid 1 (2), as presented in figure 2(*g*). The RW_4 accelerate UI before the CW_2 arrive at UI in this work, generating the rarefaction waves RW_5 which move downstream to stretch DI, as shown in figure 2(*h*). Subsequently, the rarefaction waves RW_6 and RW_7 are formed after the CW_2 accelerate UI and DI, respectively, as sketched in figure 2(*i*). Finally, the RW_7 interact with UI and the rarefaction waves RW_8 moving to DI are reflected, as presented in figure 2(*j*). After the RW_8 stretch DI, additional reverberating waves affecting the perturbation growth at either UI or DI are ignored in this work.

https://doi.org/10.1017/jfm.2025.10281 Published online by Cambridge University Press

Compared with TS_1 and the RW_1, the reverberating waves in figures 2(*f*)–2(*j*) are much weaker and thus are not considered to induce a rarefaction or compression effect on the shape of either UI or DI. Moreover, since the distance between UI and DI is short in this work, the duration from the CW_1 accelerating UI to the RW_8 interacting with DI is short, and the processes described in figures 2(*f*)–2(*j*) are considered instantaneous. In other words, from the CW_1 arriving to the RW_7 (RW_8) leaving, the amplitude variation of UI (DI) can be ignored. Therefore, after defining Δu_{1C} (Δu_{2C}) as the sum of the jump velocities of UI accelerated by the CW_1, RW_4, CW_2, RW_7 (jump velocities of DI accelerated by the CW_1, RW_5, CW_2, RW_8), based on (2.1)–(2.2), the perturbation growth rates at UI ($\dot{a}_{1C}$) and DI ($\dot{a}_{2C}$) induced by the reverberating waves in figures 2(*f*)–2(*i*) can be calculated by

$$\begin{aligned}&\dot{a}_{1C}[\rho_{1C}+\rho_{2C}\tanh(kW_C/2)]+\dot{a}_{2C}[\rho_{3C}+\rho_{2C}\tanh(kW_C/2)]\\&\quad=k(\rho_{2C}-\rho_{1C})a_{1C}\Delta u_{1C}+k(\rho_{3C}-\rho_{2C})a_{2C}\Delta u_{2C},\end{aligned}\tag{2.3}$$

$$\begin{aligned}&\dot{a}_{1C}[\rho_{1C}+\rho_{2C}\coth(kW_C/2)]-\dot{a}_{2C}[\rho_{3C}+\rho_{2C}\coth(kW_C/2)]\\&\quad=k(\rho_{2C}-\rho_{1C})a_{1C}\Delta u_{1C}-k(\rho_{3C}-\rho_{2C})a_{2C}\Delta u_{2C}.\end{aligned}\tag{2.4}$$

Here, ρ_{1C}, ρ_{2C} and ρ_{3C} are the densities of fluid 1, fluid 2 and fluid 3 after the RW_8 interact with DI; W_C is the distance between UI and DI after the CW_1 accelerate DI; and a_{1C} and a_{2C} are the amplitudes of UI and DI, respectively, just prior to the CW_1 acceleration. The expressions of W_C, a_{1C} and a_{2C} are deduced in Appendix A. Combining (2.1)–(2.2) with (2.3)–(2.4), the amplitude growth rates of UI and DI after the RW_8 pass through DI can be predicted as

$$\begin{cases}\dot{a}_1=\dot{a}_{11}+\dot{a}_{1C},\\ \dot{a}_2=\dot{a}_{21}+\dot{a}_{2C}.\end{cases}\tag{2.5}$$

We emphasise that the wave–interface interactions in figure 2 represent a continuous physical process spanning panels (*a*) to (*j*). While the incident shock initially traverses the dual-layer interface, reverberating waves persistently interact with all three interfaces. To enable systematic analysis, we strategically dissect this continuum into two sequential phases, i.e. from figures 2(*a*) to 2(*e*) and from panels (*f*) to (*j*). According to (2.5), the relationship between $\dot{a}_{11}$ and $\dot{a}_{1C}$ ($\dot{a}_{21}$ and $\dot{a}_{2C}$) determines the amplitude growth of UI (DI) of the shocked dual layer.

2.2. *Possibility analysis*

In previous works (Merritt *et al.* 2023; Zhai *et al.* 2025), it was demonstrated that, accelerated by two co-propagating shocks, the perturbation growth of a heavy-light interface can be manipulated and even freeze out can be achieved by choosing a suitable time interval between two successive shock impacts. In this work, as detailed in § 2, UI undergoes sequential acceleration by a primary shock and the following co-propagating compression waves (CW_1 and CW_2), and DI is also accelerated by the co-directional CW_1 and CW_2. Since the accelerations of both UI and DI induced by the primary shock and subsequent compression waves resemble those caused by two co-propagating shocks, this configuration enables manipulation of perturbation growth at both heavy-light interfaces. Distinct perturbation growth behaviours at UI and DI can be achieved by modulating the time interval between shock and compression wave impacts through adjustments

https://doi.org/10.1017/jfm.2025.10281 Published online by Cambridge University Press

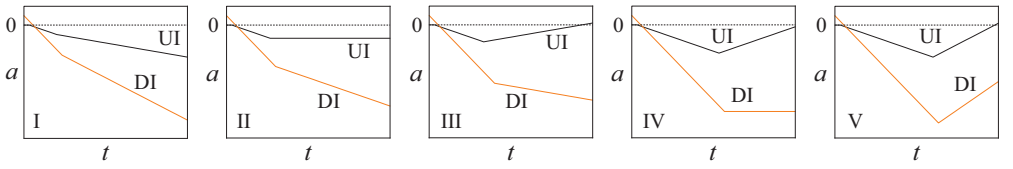


Figure 3. Schematics of the temporal evolution of UI and DI amplitudes, representing the distinct manipulation possibilities of the instability for a shocked dual layer with a AI and two successive heavy-light interfaces.

to L_0. Note that changing L_0 is equivalent to changing the shock-to-shock timing in laser experiments (Merritt *et al.* 2023) and shock-tube experiments (Zhai *et al.* 2025).

Besides the dominant successive compression waves, the reverberating rarefaction waves between UI and DI, which result from the interactions of CW_1 and CW_2 with UI and DI, can also change the perturbation growth. Systematic adjustment of wave–interface timing (via initial layer spacing L_0) theoretically permits nine perturbation growth regimes, analogous to a double-shocked heavy layer dynamics (Chen *et al.* 2025). However, in the first sub-process, the single-mode DI, accelerated by TS_1 and RW_2, exhibits a greater amplitude growth rate compared with UI which is driven solely by RW_1. This asymmetry of UI and DI precludes the realisation of four regimes (where the direction modulation of DI amplitude growth occurs prior to UI growth state reversal), thereby reducing the viable scenarios to five, as shown in figure 3. In addition, after the RW_1 stretch UI, the amplitude of UI has an opposite phase to that of the initial DI. Because DI will experience a phase inversion, the amplitudes at UI and DI will finally develop with the same phase prior to the compression waves' arrival. Under constant W_0, as L_0 increases, the five distinct possibilities of perturbation growth at UI and DI are illustrated in figure 3, which actually shows schematically the temporal evolution of UI and DI amplitudes. For convenient discussion, the initial amplitude of DI (a_{2-}) is assumed positive and thus $\dot{a}_{11} < 0$ and $\dot{a}_{21} < 0$.

Possibility I: when L_0 is insufficient, the temporal separation between the TS_1 and CW_1 impacts at the two heavy-light interfaces becomes critically short. Under this condition, the perturbation growth rate of UI accelerated by the CW_1, RW_4, CW_2 and RW_7 is smaller than that accelerated by the RW_1 in magnitude ($\dot{a}_{1\mathrm{C}} < -\dot{a}_{11}$), and the perturbation growth rate of DI accelerated by the CW_1, RW_5, CW_2 and RW_8 is smaller than that accelerated by the RW_2 and TS_1 in magnitude ($\dot{a}_{2\mathrm{C}} < -\dot{a}_{21}$). As a result, the perturbation growth at both UI and DI cannot be reversed by the reverberating waves in the second sub-process, and the amplitudes of both UI and DI grow with the opposite phase to a_{2-} ($\dot{a}_1 < 0$ and $\dot{a}_2 < 0$).

Possibility II: as L_0 increases, the time interval between TS_1 and CW_1 interacting with the two heavy-light interfaces is prolonged, and the UI will obtain a larger amplitude when it is impacted by the compression waves. There is a special L_0 at which the perturbation growth rate of UI accelerated by the reverberating waves in the second sub-process equals the amplitude growth rate of UI just prior to CW_1 arriving. Consequently, the perturbation growth at UI is frozen after the RW_7 pass through UI ($\dot{a}_{1\mathrm{C}} = -\dot{a}_{11}$, i.e. $\dot{a}_1 = 0$). Before the compression waves arrive, as mentioned, the growth rate of the perturbation at DI is much more significant than that at UI and more difficult to cancel. As a result, when L_0 satisfies the conditions of freezing the UI amplitude growth, the perturbation at DI still evolves with the opposite phase to a_{2-} ($\dot{a}_2 < 0$).

Possibility III: when L_0 is further raised, the effect of reverberating waves in the second sub-process can reverse the UI amplitude evolution, i.e. there is a phase reversal for the

https://doi.org/10.1017/jfm.2025.10281 Published online by Cambridge University Press

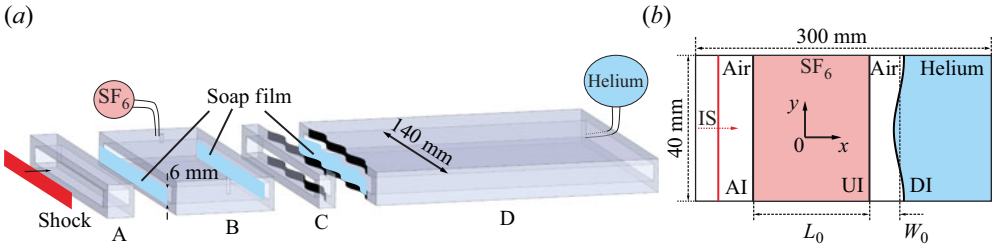


Figure 4. (*a*) Schematic of the interface formations by the soap-film technique, and (*b*) the sketch of the computational domain for a flat shock interacting with a dual layer with a flat AI, an undisturbed UI, and a disturbed DI. L_0 (W_0), the initial distance between AI and UI (UI and DI); IS, the incident shock.

perturbation at UI after it is accelerated by the CW_1, RW_4, CW_2 and RW_7, and the UI amplitude grows with the same phase as a_{2-} ($\dot{a}_1 > 0$). However, L_0 is still not large enough to freeze DI amplitude growth, and the perturbation at DI performs similarly to that of possibility II ($\dot{a}_2 < 0$). As a result, the perturbations at UI and DI grow in opposite directions.

Possibility IV: when L_0 reaches another special value that is large enough, the perturbation growth at DI can be frozen. In this situation, because the perturbation growth at UI is much slower than that at DI before the CW_1 arrive, the perturbation growth of UI is reversed by the CW_1, RW_4, CW_2 and RW_7. The perturbation growth at UI is similar to that of possibility III ($\dot{a}_1 > 0$), but growth stagnation is achieved at DI after the RW_8 impact DI ($\dot{a}_2 = 0$, i.e. $\dot{a}_{2C} = -\dot{a}_{21}$).

Possibility V: if L_0 exceeds the special value in possibility IV, the perturbation growth at DI is reversed by the CW_1, RW_5, CW_2 and RW_8. In this situation, the amplitude variations of both UI and DI are reversed after the reverberating waves considered in figure 2(*f–j*) interact with the two interfaces, and both the perturbations at UI and DI evolve with the same phase as a_{2-} ($\dot{a}_1 > 0$ and $\dot{a}_2 > 0$).

3. Experimental and numerical methods

3.1. *Experimental methods*

The experimental configuration employs an advanced soap-film technique (Liu *et al.* 2018*a*; Chen *et al.* 2024*b*) to establish precisely defined discontinuous interfaces in the dual-layer system, complemented by superhydrophobic–oleophobic surface confinement (Li *et al.* 2023). As presented in figure 4(*a*), four transparent devices (A–D), with a width of 140 mm and a height of 6 mm, are first manufactured using acrylic plates. Two flat soap-film interfaces are formed at both sides of device B, and a single-mode soap-film interface is created at the upstream side of device D. Then SF_6 is pumped into device B to replace air, and helium is pumped into device D from its end. Thus, a dual-layer, with an unperturbed air–SF_6 interface (AI), a flat SF_6air interface (UI) and a single-mode air–helium interface (DI), is created in the shock tube.

The experiments are conducted in a horizontal shock tube (Liu *et al.* 2018*a*; Chen *et al.* 2024*b*). The Mach number of the incident shock when it interacts with AI is 1.26. The perturbation wavelength (λ) is fixed as 40 mm, and the initial amplitude of DI satisfies the small amplitude assumption ($ka_{2-} = 0.1$). Schlieren photography combined with a high-speed camera (FASTCAM SA-Z, Photron Ltd) is used to record the post-shock flow field in our experiments. The frame rate of the camera is 50 400 frames per second, and the exposure time is 0.35 μs. The spatial resolution of the schlieren image is

https://doi.org/10.1017/jfm.2025.10281 Published online by Cambridge University Press

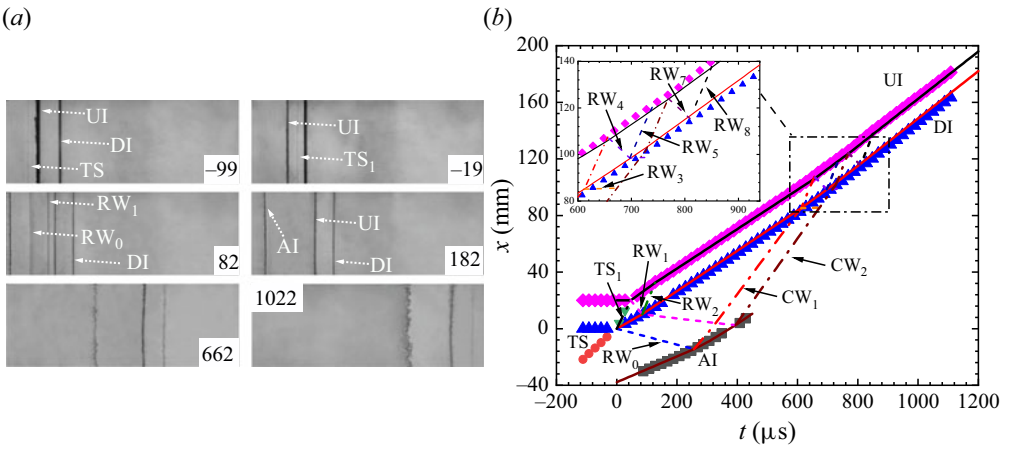


Figure 5. (*a*) Schlieren images of an undisturbed dual layer accelerated by the incident shock, and (*b*) the trajectories of the interfaces and waves. Symbols and lines indicate experimental and theoretical results, respectively. The numbers in (*a*) denote the time in μs. The abbreviations have the same meaning as those in figure 2.

0.27±0.01 mm pixel^{-1}. The ambient pressure and temperature are 101.3±0.1 kPa and 297.9±1 K, respectively. The boundary layer effect was discussed by Liu *et al.* (2018*a*), and can be ignored.

3.2. *One-dimensional experiment for determining the volume fractions*

To determine the volume fractions of air, SF_6 and helium in different regions of the dual-layer configuration, a one-dimensional (1-D) experiment of a shock wave interacting with a dual layer with three unperturbed interfaces is first performed. The experimental schlieren images showing the development of an undisturbed dual layer with $L_0 = 70$ mm and $W_0 = 20$ mm after shock impact are presented in figure 5(*a*). The initial time is defined as the moment when TS_1 meets DI in experiments and computations hereafter. When UI is accelerated by the first transmitted shock TS, a transmitted shock TS_1 is generated in air and moves to DI (−19 μs). After TS_1 interacts with DI, the rarefaction waves RW_0 formed by TS reflecting from UI and the RW_1 generated by TS_1 reflecting from DI are both observed in experimental images (82 μs). The transmitted shock TS_2 moving in helium and other reverberating waves described in figure 2 cannot be captured in experiments due to the low density of helium and the weak intensities of these waves. At 182 μs, the shocked AI can be captured and the three interfaces of the dual layer all remain almost flat in experiments. After AI passes through the initial positions of UI and DI, small perturbations also arise at AI. However, both UI and DI remain unperturbed, which indicates that the interface coupling induced by AI can be ignored (662–1022 μs). As time elapses, DI becomes obscure due to the molecular mixing of air with helium (1022 μs).

The trajectories of waves and interfaces extracted from the experimental high-speed diagnostics and predicted by 1-D theory are compared in figure 5(*b*). Quantitative agreement between experimental measurements and theoretical predictions emerges when the accelerations induced by the reverberating waves mentioned in figure 2 are quantified for the motions of UI and DI. This validation confirms that other reflected waves absent in figure 2 contribute negligibly to the interfacial dynamics, and their effects are thereby ignored in the modelling frameworks. From the comparison between experimental results and prediction of 1-D theory, the volume fractions of specific gases can be obtained. In this

https://doi.org/10.1017/jfm.2025.10281 Published online by Cambridge University Press

v_1^{TS}	v_2^{TS}	Δu_1	Δu_2	Δu_{R1}	Δu_{R2}	Δu_{1C}	Δu_{2C}	c_1	c_2	c_3	c_4
430.11	805.19	120.31	153.24	21.94	−14.05	25.23	28.08	375.19	368.55	366.33	366.95
u_{C1}	γ_{20}	ρ_{2-}	ρ_{2+}	ρ_{3-}	ρ_{3+}	ρ_1	ρ_2	ρ_3	ρ_{1C}	ρ_{2C}	ρ_{3C}
153.45	1.40	1.16	1.47	0.33	0.41	7.16	1.44	0.40	7.64	1.45	0.42

Table 1. Theoretical parameters in undisturbed case: v_1^{TS} and v_2^{TS} are the velocities of the TS_1 and TS_2; Δu_1 (Δu_2), Δu_{R1} (Δu_{R2}) and Δu_{1C} (Δu_{2C}) are the jump velocities of UI (DI) induced by TS (TS_1), the RW_1 (RW_2) and reverberating waves after the CW_1, respectively; c_1 and c_2 are the sound speeds of fluid 2 before and after being accelerated by the RW_1, respectively; c_3 (c_4) are the sound speeds of fluid 2 near UI (DI) after being accelerated by the RW_1 (RW_2); u_{C1} is the velocity of UI being accelerated by the CW_1 but not being accelerated by the RW_4; γ_{20} is the adiabatic exponent of the fluid 2; ρ_{2-} (ρ_{3-}) and ρ_{2+} (ρ_{3+}) are the densities of fluid 2 (3) near DI before and after being accelerated by TS_1. ρ_1 (ρ_{1C}), ρ_2 (ρ_{2C}) and ρ_3 (ρ_{3C}) are the densities of fluid 1, 2 and 3, respectively, after DI impacted by the RW_2 (after the RW_8 impacting DI). The units of velocity and density are m s^{-1} and kg m^{-3}, respectively.

work, the volume fraction of air (helium) in fluid 0 is 99.5 % (0.5 %), the volume fraction of SF_6 (air) in fluid 1 is 90.1 % (9.9 %), the volume fraction of air (helium) in fluid 2 is 98.0 % (2.0 %) and the volume fraction of helium (air) in fluid 3 is 83.3 % (16.7 %). Note that, in all experimental trials, we maintain constant injection rates and durations for both helium and SF_6 to achieve comparable volume fractions within the test section. For the layer with variable width (L_0) between AI and UI, the SF_6 injection parameters are calibrated to approach almost 100 % concentration when L_0 is maximised. However, due to sequential gas charging (SF_6 first followed by helium) and associated diffusion during the helium injection phase, the SF_6 concentration in fluid 2 inevitably decreases below saturation levels prior to shock wave arrival. The velocities required for the theoretical calculations in § 2 are calculated by 1-D theory and are provided in table 1. The specific times in this work can be calculated by combining the velocities in table 1 with L_0 and W_0. Due to the same experimental methods being used for different cases, the parameters given in table 1 are considered as the initial parameters in the following disturbed cases for both the experiments and numerical simulations.

3.3. *Numerical scheme and set-up*

Numerical simulations are performed to capture more details of a shock interacting with a dual layer and to explore the effects of the initial conditions. The compressible two-dimensional (2-D) multi-component non-reactive Euler equations are adopted to describe the flow. The governing equations in conservative form are expressed as

$$\frac{\partial \rho}{\partial t} + \nabla \cdot (\rho \boldsymbol{u}) = 0, \tag{3.1}$$

$$\frac{\partial \rho \boldsymbol{u}}{\partial t} + \nabla \cdot (\rho \boldsymbol{u} \otimes \boldsymbol{u} + p\boldsymbol{\delta}) = 0, \tag{3.2}$$

$$\frac{\partial \rho E}{\partial t} + \nabla \cdot [(\rho E + p)\boldsymbol{u}] = 0, \tag{3.3}$$

$$\frac{\partial \rho Y_l}{\partial t} + \nabla \cdot (\rho Y_l \boldsymbol{u}) = 0 \quad (l = 1, \ldots, N-1), \tag{3.4}$$

where ρ, $\boldsymbol{u} = [u, v]^t$, p, E and Y_l stand for the density, velocity vector, pressure, total energy per unit mass of the mixture and mass fraction of species l, respectively; $\otimes$

https://doi.org/10.1017/jfm.2025.10281 Published online by Cambridge University Press

and $\boldsymbol{\delta}$ are the tensor product the Kronecker delta, respectively. The equation of state is expressed as

$$E = \frac{p}{\rho(\gamma - 1)} + \frac{1}{2}\boldsymbol{u} \cdot \boldsymbol{u}, \tag{3.5}$$

where γ refers to the specific heat ratio of the mixture and is calculated by

$$\gamma = \frac{\sum \dfrac{Y_l \gamma_l}{M_l(\gamma_l - 1)}}{\sum \dfrac{Y_l}{M_l(\gamma_l - 1)}}, \tag{3.6}$$

with γ_l and M_l being the specific heat ratio and molar mass of species l, respectively. In this work, four species, N_2, O_2, helium and SF_6, are considered. In the simulations, $\gamma_1 = 1.4005$, $M_1 = 28.0134$ g mol^{-1} are adopted for N_2, $\gamma_2 = 1.3956$, $M_2 = 31.9988$ g mol^{-1} for O_2, $\gamma_3 = 1.6667$, $M_3 = 4.0026$ g mol^{-1} for helium and $\gamma_4 = 1.094$, $M_4 = 146.055$ g mol^{-1} for SF_6. Air is considered as the mixture of N_2 with volume fraction of 79 % and O_2 with volume fraction of 21 %.

In the simulations, the numerical scheme high-order weighted essentially non-oscillatory (WENO) and double flux (HOWD) (Ding *et al.* 2017) is employed. The fifth-order WENO construction (Jiang & Shu 1996) is combined with the multi-component double-flux algorithm (Abgrall & Karni 2001; Billet & Abgrall 2003) to capture material interfaces and wave patterns with high resolution and high-order accuracy. The third-order total variation diminishing Runge–Kutta scheme is used for time advancing. The HOWD has demonstrated accuracy and reliability for simulating a shock wave interacting with gas interfaces (Ding *et al.* 2017; Cao *et al.* 2024; Li *et al.* 2024), and for more details about the scheme the reader can refer to the work of Ding *et al.* (2017). The validity of the numerical methods will also be verified later through experiments.

The initial configuration for the 2-D numerical simulations, faithfully replicating the experimental geometry, is shown in figure 4(*b*). The inlet and outlet boundary conditions are enforced at the left and right boundaries, respectively, whereas periodic boundary conditions are imposed at the upper and lower boundaries. The widths of the computational domain in the x and y directions are 300 and 40 mm (the perturbation wavelength), respectively. The intensity of the IS, ambient pressure and temperature are set according to the experimental values in § 3.1. The volume fractions of specific gases in the domains of the numerical flow are enforced as the 1-D experimental result in § 3.2.

3.4. *Code validation*

One shock-tube experiment with the initial parameters of $ka_{1+} = 0$ ($ka_{2-} = 0.1$), $W_0 = 10$ mm and $L_0 = 57.2$ mm is conducted to verify the numerical methods. The rationale behind this parameter selection will be systematically elucidated in the subsequent section. In this case, growth stagnation of the perturbation at DI is expected by the theory proposed in § 2. Comparison of the perturbation developments at UI and DI between experiment and computation is provided in figure 6. After UI and DI are both accelerated by the shock waves, their amplitudes begin to vary and the shocked AI remains flat in the observation region (201 μs). Because only the perturbation developments at UI and DI are considered in this work, the moving AI are removed in the following schlieren images. From 381 to 581 μs, the perturbation amplitude at DI grows significantly. However, after 581 μs, the perturbation amplitude of DI is almost unchanged. The results show that growth stagnation of the amplitude at DI is realised. The morphologies of both

https://doi.org/10.1017/jfm.2025.10281 Published online by Cambridge University Press

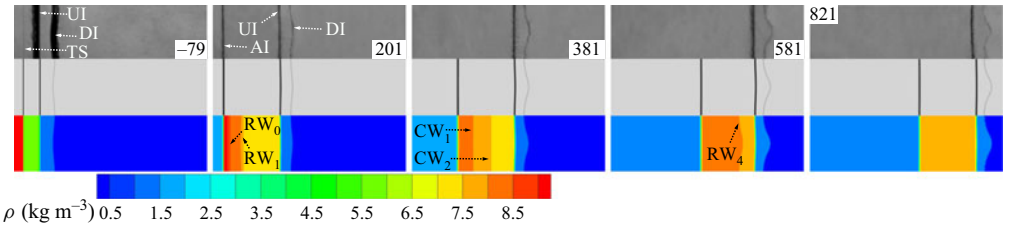


Figure 6. Comparison between the experimental schlieren (top) and numerical schlieren (middle) images, and density contour images (bottom) from the computation for case 10-57.2. Numbers in the top panels denote time in μs.

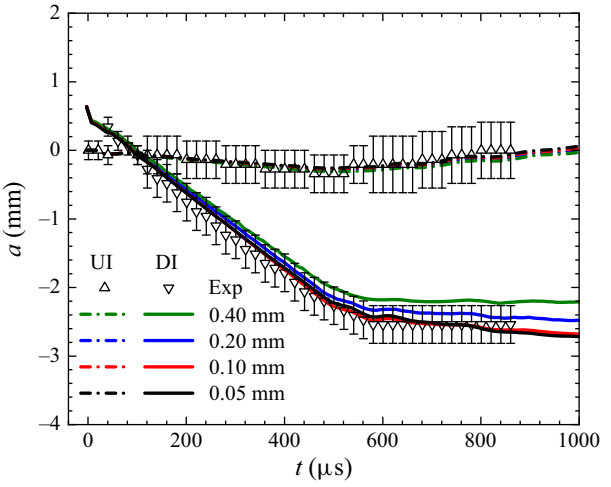


Figure 7. Comparison of the amplitude variation of UI and DI for case 10-57.2 between experimental and the numerical results. Code validation is also conducted here based on four kinds of mesh sizes. Symbols (Lines) represent experimental (numerical) results.

UI and DI in the numerical simulation are consistent with their experimental counterparts, which qualitatively validates the numerical methods. Moreover, the density contours from the computation are given in figure 6 to clearly demonstrate the reverberating waves in the shocked dual layer. In numerical simulation, the RW_0 and RW_1 moving towards AI can be observed (201 μs), and then the CW_1 (CW_2) are formed by the RW_0 (RW_1) reflecting from AI (381 μs). When UI and DI are both accelerated by the CW_1 and CW_2, only the reflected rarefaction waves RW_4 can be observed (581 μs). In the late stage, there are no obvious reverberating waves in the flow field (821 μs). We emphasise two experimental constraints: first, the small amplitude variation of UI cannot be precisely captured due to the limited spatial resolution of the schlieren image (approximately 0.27 mm); second, the progressive contrast loss of DI during the evolution, attributable to the molecular mixing, makes it difficult to observe DI clearly at the late stages. As a result, only one experiment in this work is conducted to realise the growth stagnation of perturbation at DI, and simultaneously to verify the numerical methods. In the following, extensive numerical simulations will be performed to validate the model.

The temporal amplitudes of UI and DI are extracted from the experimental images for code validation and grid convergence evaluation, as shown in figure 7. In the simulations, the nodes with a volume fraction of SF_6 45 % are chosen as AI and UI, and the nodes with a

https://doi.org/10.1017/jfm.2025.10281 Published online by Cambridge University Press

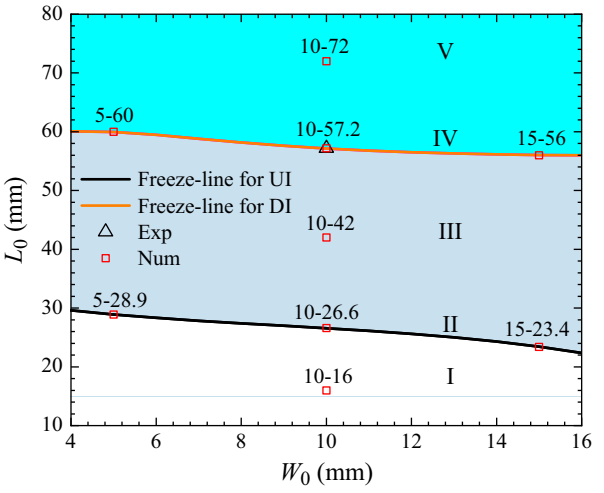


Figure 8. Distribution of the manipulation possibilities of the perturbation growth at UI and DI in (W_0, L_0) domain. Triangle and square points represent the experiment and computations designed specifically, respectively. The roman numerals I–V refer to the five manipulation possibilities, as schematically shown in figure 3, and the perturbation growth stagnation is achieved at UI (II) and DI (IV), respectively.

volume fraction of helium 41.7 % are chosen as DI. These threshold values are determined by averaging the value fractions of the specific gases at both sides of the interface. Four different initial mesh sizes of 0.40, 0.20, 0.10 and 0.05 mm are examined in numerical simulations. As shown in figure 7, the interface amplitudes converge and agree well with the experimental results when the mesh size is reduced to 0.10 and 0.05 mm. To save the computational cost but ensure accuracy, the initial mesh size of 0.10 mm is adopted in this work.

4. Result and discussion

According to the theoretical models in § 2 and the 1-D parameters in § 3, the relationships between W_0 and L_0 under conditions $\lambda = 40$ mm, $a_{1+} = 0$ mm and $ka_{2-} = 0.1$, are established to realise perturbation growth stagnation at either UI or DI, as visualised in figure 8. These two lines are defined as the freeze lines in this work, and freezing perturbation can be realised at either UI or DI when the (W_0, L_0) coordinate locates at these two characteristic curves. There are no intersection points between the two freeze lines, which indicates that the concurrent perturbation growth stagnation at both UI and DI is theoretically unattainable. These two curves distinguish the five different manipulation possibilities of the perturbation growth at UI and DI, as demonstrated in figure 3. To verify the model, numerical simulations are carried out extensively to realise different manipulation possibilities. According to figure 8, five cases with the same W_0 but different L_0 are first chosen to realise different possibilities at UI and DI. Subsequently, six additional cases with independent W_0–L_0 combinations are designed to validate the model's predictive capability for achieving growth stagnation at a shocked dual layer. In the following, the numerical cases are named W_0–L_0, as shown in figure 8.

4.1. *Perturbation growths for successive interfaces with the same W_0 but different L_0*

The numerical simulations are carried out to validate the predictive ability of the model (2.5) in determining the different possibilities of the perturbation growth at both

https://doi.org/10.1017/jfm.2025.10281 Published online by Cambridge University Press

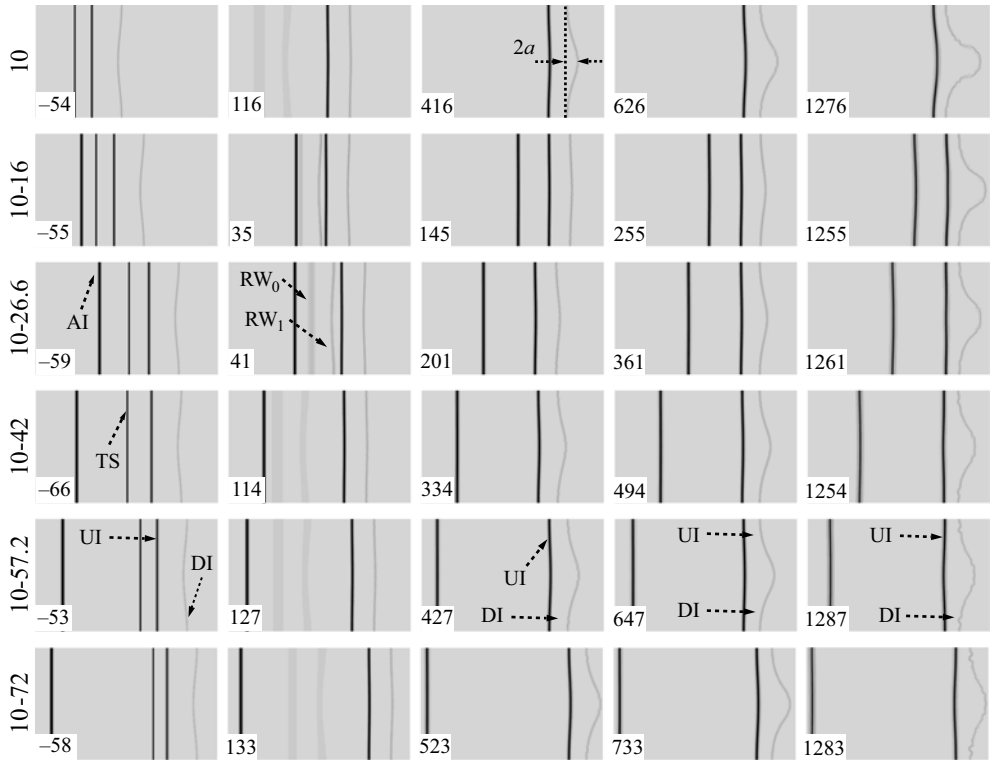


Figure 9. Schlieren images of the shock-induced dual-layer evolution for different numerical cases with the same $W_0 = 10$ mm but different L_0. Numbers in the lower left corner of the schlieren images denote time in μs. The symbols have the same meaning as those in figure 6.

UI and DI. The numerical schlieren images of the shocked dual layers in five cases sharing identical $W_0 = 10$ mm but varying L_0 are shown in figure 9. These five cases correspond to the five different possibilities described in figure 8. The baseline case (labelled 10) establishes a reference configuration without AI and maintains the other parameters equivalent to the cases named 10-L_0. The amplitude growth rate of the perturbation at DI exhibits great diversity among different cases, which qualitatively demonstrates that the perturbation of a shocked dual layer can be manipulated simply by changing the distance between the interfaces. Although the perturbation amplitude of UI is comparatively small, the slight trend that the UI amplitude grows in the opposite phase to the DI amplitude as L_0 increases can be observed.

Figure 10 illustrates the temporal evolution of DI and UI amplitudes, comparing numerical results with analytical predictions from model (2.5). Following the definition established in § 2, the initial DI amplitude (a_{2-}) is defined as positive and thereby the initial perturbation growth phase is negative. After the CW_1 impact, as L_0 increases, the phase of perturbation at UI experiences a transition from negative to positive. Specifically, for case 10-26.6, growth stagnation is realised at UI. After the CW_2 impact, the reduced amplitude growth rates of DI in cases 10-16, 10-26.6, and 10-42 are compared with the counterpart in baseline case 10, and the amplitude of DI in these three cases develops more slowly as L_0 increases. Notably, case 10-57.2 exhibits near-stagnant DI amplitude variation, whereas case 10-72 demonstrates slight DI amplitude reduction. To sum up, different manipulation possibilities illustrated in figure 3 can be achieved by fixing W_0

https://doi.org/10.1017/jfm.2025.10281 Published online by Cambridge University Press

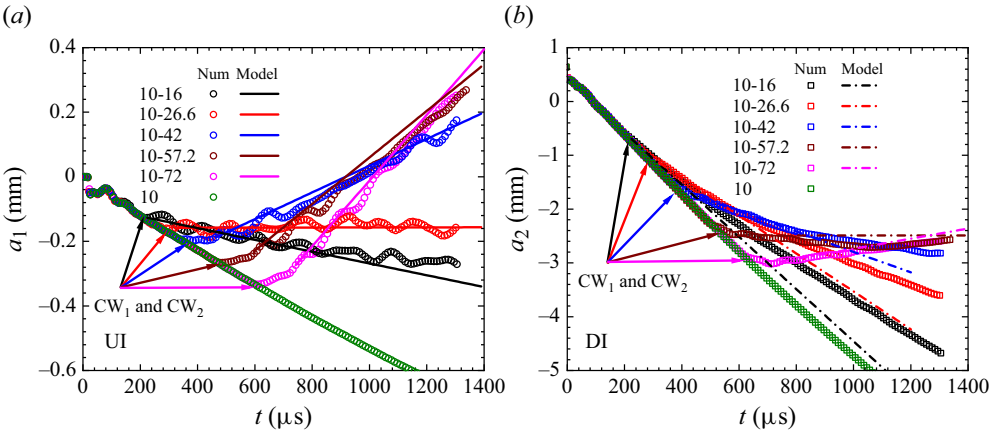


Figure 10. Comparison of the amplitudes of UI (*a*) and DI (*b*) obtained from numerical and theoretical results in cases with fixed $W_0 = 10$ mm. Here, the initial time is the moment when the transmitted shock TS_1 interacts with DI.

but varying L_0. Note that the UI is initially flat in these cases, the effect of the initial UI amplitude on the perturbation growth of DI is discussed in Appendix B.

The lines in figure 10 represent the theoretical predictions of the perturbation amplitude by models (2.1)–(2.5) after the reverberating waves impact the two interfaces. An exception occurs in case 10-72, where the pre-CW_1 DI amplitude violates the small amplitude hypothesis ($ka_{2C} = -0.53$). Therefore, for case 10-72, the amplitude growth rate of DI ($\dot{a}_2$) in the model (2.5) needs to be revised as

$$\dot{a}_2 = \dot{a}_{21} + R \cdot \dot{a}_{2C}, \tag{4.1}$$

where $R = 1/(1 + (ka_{2C}/3)^{(4/3)})$ is the reduction factor proposed by Dimonte & Ramaprabhu (2010). In figure 10, the amplitude variations of UI and DI for all cases generally coincide well with the predictions by the model in the early stage of the evolution of the interfaces impacted by the CW_1. This agreement validates the predictive capacity of model (2.5) under linear growth conditions. The gradually emerging deviation between the predictions and numerical simulations in figure 10(*b*) is caused by the nonlinear growth of the DI amplitude, since model (2.5) only considers the linear growth of the DI and UI amplitudes.

4.2. *Growth stagnation of successive interfaces with different distances*

In this subsection, numerical simulations are carried out to validate the model (2.5) in predicting the growth stagnation conditions at either UI or DI. According to figure 8, we extend the investigation beyond the previously analysed cases 10-26.6 and 1057.2 to incorporate four configurations: two configurations (cases 5-60 and 15-56) targeting DI amplitude stagnation and two configurations (cases 5-28.9 and 15-23.4) for the realisation of growth stagnation at UI. The numerical schlieren images for these four cases are shown in figure 11. Qualitatively, from the last two images in cases 5-60 and 15-56, the amplitude variation of DI almost stagnates, and in cases 5-28.9 and 15-23.4, the amplitude change of UI cannot be clearly observed, but the DI amplitude grows significantly.

Time variations of UI and DI amplitudes are given in figure 12, together with the numerical results from case 10 for comparison. The quantitative data reveal that the amplitude growth stagnation is realised at either UI or DI under the given initial conditions. The lines in figure 12 represent the linear growth of the interface amplitude predicted

https://doi.org/10.1017/jfm.2025.10281 Published online by Cambridge University Press

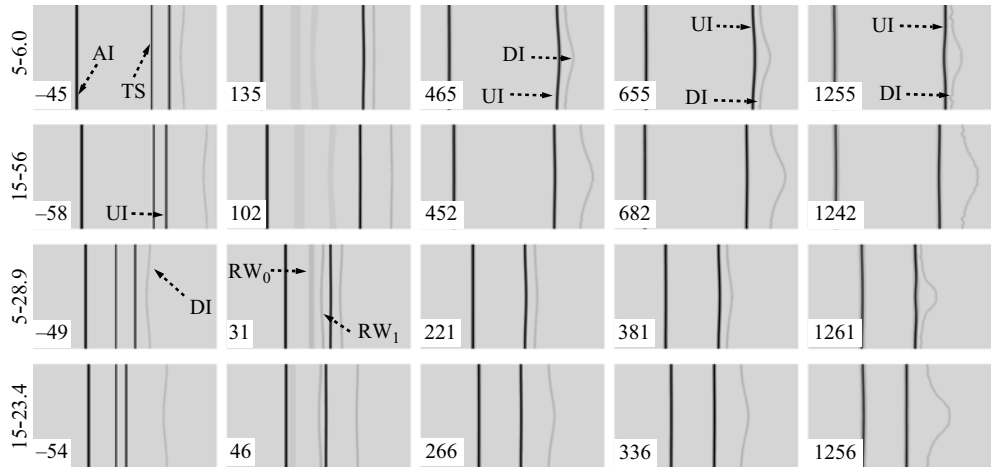


Figure 11. Numerical schlieren images of the shock-accelerated dual-layer evolution for different cases designed to realise individual stagnation of amplitude at UI or DI. Numbers in the lower left corner of the schlieren images denote time in μs. The symbols have the same meaning as those in figure 9.

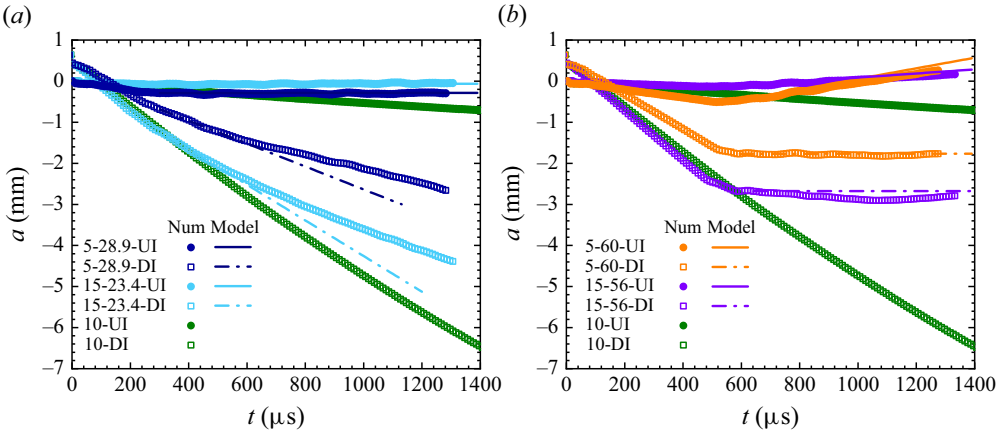


Figure 12. Numerical verification of the model (2.5) in predicting the growth stagnation conditions at UI (*a*) and at DI (*b*).

by (2.5), which coincide well with the numerical results. To sum up, the model (2.5) can well predict the conditions of growth stagnation at either DI or UI when the dual layer has different L_0 and W_0.

5. Conclusions

The modulation of perturbation growth at successive heavy-light interfaces in a shock-accelerated dual layer holds critical importance for mitigating hydrodynamic instabilities in ICF. Unlike single-layer systems, dual-layer configurations introduce a complex reverberating wave dynamics that significantly influences interface evolution. This work systematically investigates these interactions, revealing that reflected compression waves, propagating co-directionally with the incident shock, enable the targeted manipulation of perturbation growth at the two successive heavy-light interfaces. Then, we develop an analytical model integrating both wave-reverberation and interface-coupling effects to

https://doi.org/10.1017/jfm.2025.10281 Published online by Cambridge University Press

quantify linear growth rates at the two interfaces. For configurations with only an initially perturbed downstream interface, the model identifies five distinct perturbation growth regimes. Crucially, these regimes can be selectively controlled by changing the initial distances between the interfaces of the layer, offering flexibility in instability manipulation for a dual-layer relevant to classical ICF capsule.

The model further quantifies the parametric thresholds required for growth stagnation at either an upstream or downstream heavy-light interface. To validate these theoretical predictions, both shock-tube experiments and numerical simulations are carried out. The results show that the five different manipulation possibilities of the perturbation growth are all realised under the initial parameter conditions designed by the model. Specifically, growth stagnation of the perturbation at the upstream or downstream heavy-light interface is also realised for different initial conditions designed based on the model.

These findings advance the mechanistic understanding of hydrodynamic instability control in shock-accelerated multi-interface systems, with direct implications for ICF capsule optimisation. While this study resolves a single-mode perturbation dynamics, future investigations will address the modulation of multi-mode perturbations in shocked multi-interface systems.

Funding. This work was supported by the National Natural Science Foundation of China (Nos. 12388101, 12372281, 12102425 and 123B2034), the Strategic Priority Research Program of Chinese Academy of Sciences (No. XDB0620201) and Youth Innovation Promotion Association CAS.

Declaration of interests. The authors report no conflict of interest.

Appendix A. Derivations of the model and parameters

In this appendix, the detailed derivations of (2.1)–(2.5) and the relevant parameters are presented. After the incident shock interacts with AI, TS is generated and moves to UI, as shown in figure 2(*a*). Then the flat UI is accelerated and TS_1 is generated in fluid 3, as shown in figure 2(*b*). The perturbation at DI is first compressed by TS_1, and its amplitude can be expressed as

$$a_{2+} = a_{2-}\left(1 - \Delta u_2 / v_1^{TS}\right), \tag{A1}$$

where a_{2-} (a_{2+}) is the DI amplitude before (after) it is accelerated by TS_1; Δu_2 and v_1^{TS} are the jump velocity of DI induced by TS_1 and velocity of TS_1, respectively. After DI is accelerated by TS_1, the perturbed rarefaction waves RW_1 are reflected, as shown in figure 2(*c*). When the RW_1 form, their amplitudes are

$$\begin{cases} a_{Rf1}^0 = a_{2-}\left(1 + (c_1 - \Delta u_1)/v_1^{TS}\right), \\ a_{Rt1}^0 = a_{2-}\left(1 + (c_2 - \Delta u_2)/v_1^{TS}\right), \\ a_{R1}^0 = \left(a_{Rf1}^0 + a_{Rt1}^0\right)/2. \end{cases} \tag{A2}$$

Here, a_{Rf1}^0, a_{Rt1}^0 and a_{R1}^0 are the initial amplitude of the RW_1 head, the initial amplitude of the RW_1 tail and the average amplitude of the RW_1, respectively; c_1 (c_2) is the sound speed of the fluid 2 between UI and the RW_1 head (between DI and the RW_1 tail); and Δu_1 is the jump velocity of UI induced by TS. According to the work of Velikovich & Phillips (1996), as the RW_1 move, the amplitude of the RW_1 head remains as a_{Rf1}^0, but the amplitude of the RW_1 tail varies. When the RW_1 interact with UI, the amplitude of the

https://doi.org/10.1017/jfm.2025.10281 Published online by Cambridge University Press

RW_1 tail can be expressed as

$$\begin{cases} a_{Rt1}^{-} = a_{\mathrm{Rt1}}^{0} + k a_{Rt1}^{0} c_1 U_{R1}, \\ U_{R1} = \sqrt{(\gamma_{20}+1)(1-c_2/c_1)(\gamma_{20}-1)}, \end{cases} \tag{A3}$$

where U_{R1} is a parameter for calculating the amplitude growth rate of the RW_1 tail, γ_{20} is the adiabatic exponent of the fluid 2 and k is perturbation wavelength. Accordingly, the average amplitude of the RW_1 arriving at UI is $a_{R1}^{-} = (a_{Rf1}^{0} + a_{Rt1}^{-})/2$.

After the RW_1 pass through the flat UI, rarefaction waves RW_2 are generated and travel to DI, as shown in figure 2(*d*). We define the time of the RW_1 impacting UI as t_1, which can be calculated as $t_1 = W_0(1 - \Delta u_1/v_1^{TS})/c_1$, where W_0 is the initial distance between UI and DI before IS interacts with the dual layer. At $t = t_1$, the RW_1 stretch the UI and introduce the perturbation to the initially flat UI. According the model proposed by Chen *et al.* (2023*a*, 2024*b*), the UI amplitude after it is just impacted by the RW_1 can be expressed as

$$a_{1R}^{+} = -a_{R1}^{-} \frac{\Delta u_{R1}}{c_1 + c_2 + \Delta u_1 - \Delta u_2}. \tag{A4}$$

After the RW_1 leave UI, interface coupling begins to affect UI and the perturbation growth at UI will be quantified later. When the RW_2 are just generated, their amplitudes can be expressed as

$$\begin{cases} a_{Rf2}^{0} = -a_{Rf1}^{0} \dfrac{c_2 + \Delta u_2 - \Delta u_1}{c_1}, \\ a_{Rt2}^{0} = -a_{Rt1}^{-} \dfrac{c_3 + \Delta u_{R1}}{c_2}, \\ a_{R2}^{0} = \left(a_{Rf2}^{0} + a_{Rt2}^{0}\right)/2, \end{cases} \tag{A5}$$

where a_{Rf2}^{0}, a_{Rt2}^{0} and a_{R2}^{0} are the initial amplitude of the RW_2 head, amplitude of the RW_2 tail and average amplitude of the RW_2, respectively; c_3 is the sound speed of fluid 2 between the RW_2 tail and UI; and Δu_{R1} is the jump velocity of the UI induced by the RW_1. Because the RW_2 intensity is weak and the duration of the RW_2 moving in fluid 2 is short, the RW_2 amplitudes are assumed to be constant before they encounter the DI.

Before the RW_2 encounter with DI, the amplitude of DI varies from a_{2+} in (A1), and needs to be determined. Note that there is a start-up process of the perturbation at the shocked DI (Li *et al.* 2024), and the start-up time τ can be expressed as

$$\tau = \frac{1}{k}\left(\frac{2 - 2A_{2+}}{\Delta u_2 + c_2 + c_1 - \Delta u_1} + \frac{1 + A_{2+}}{v_2^{TS} - \Delta u_2}\right), \tag{A6}$$

where v_2^{TS} is the velocity of TS_2; $A_{2+} = (\rho_{3+} - \rho_{2+}/\rho_{3+} + \rho_{2+})$ is the Atwood number of the DI after being impacted by TS_1; and ρ_{2+} and ρ_{3+} are the densities of fluids 2 and 3 in the vicinity of DI after being impacted by TS_1, respectively. In this work, the moment when the RW_2 arrives at DI is defined as t_2, which can be expressed as $t_2 = t_1 + W_0(1 - \Delta u_1/v_1^{TS})[1 + (\Delta u_2 - \Delta u_1)/c_1]/c_2$. If $t_2 \leqslant \tau$, when the RW_2 interact

https://doi.org/10.1017/jfm.2025.10281 Published online by Cambridge University Press

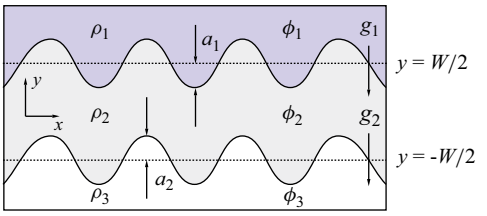


Figure 13. Schematic showing the configuration analysed using linear stability theory for the system of three different fluids, where ρ_1, ρ_2 and ρ_3 are the densities of the three fluids, and ϕ_1, ϕ_2 and ϕ_3 are the velocity potentials; a_1 and a_2 are initial interface amplitudes; g_1 and g_2 are the accelerations of the two interfaces and W is the initial distance between the two interfaces.

with DI, the amplitude of DI (a_{2R}^-) can be quantified as

$$\begin{cases} a_{2R}^- = \int_0^{t_2} \dot{a}_{20}\mathrm{d}t, \\ \dot{a}_{20} = \dfrac{2\dot{a}_2^1}{(1-A_{2+})\coth[k(\Delta u_2 + c_2 + c_1 - \Delta u_1)t/2] + (1+A_{2+})\coth[k(v_2^{TS} - \Delta u_2)t]}, \end{cases} \tag{A7}$$

where $\dot{a}_2^1 = k\Delta u_2(a_{2+}A_{2+} + a_{2-}A_{2-})/2$ is the linear growth rate of DI amplitude (a_2) induced by TS_1, and is predicted by the VMG model (Vandenboomgaerde, Mügler & Gauthier 1998), $A_{2-} = (\rho_{3-} - \rho_{2-})/(\rho_{3-} + \rho_{2-})$ is the Atwood number of DI before being impacted by TS_1, ρ_{2-} and ρ_{3-} being the densities of the fluids 2 and 3 in the vicinity of DI before being impacted by TS_1, respectively. When $t_2 > \tau$, a_{2R}^- can be expressed

$$\begin{cases} a_{2R}^- = \int_0^{\tau} \dot{a}_{20}\mathrm{d}t + (t_2 - \tau)\dot{a}_2^1, \\ \dot{a}_{20} = \dfrac{2\dot{a}_2^1}{(1-A_{2+})\coth[k(\Delta u_2 + c_2 + c_1 - \Delta u_1)t/2] + (1+A_{2+})\coth[k(v_2^{TS} - \Delta u_2)t]}. \end{cases} \tag{A8}$$

After the RW_2 pass by the interface, DI is stretched and its amplitude can be quantified as

$$a_{2R}^+ = a_{2R}^- + (a_{2R}^- - a_{R2}^0)\frac{\Delta u_{R2}}{c_2 + c_3 + \Delta u_1 + \Delta u_{R1} - \Delta u_2}. \tag{A9}$$

The perturbation growth at UI will be affected by interface coupling after the RW_1 pass through UI, and the perturbation growth at DI will be affected by interface coupling after the RW_2 pass through DI. Considering three different incompressible and irrotational fluids separated by two interfaces with a distance W, as shown in figure 13, Liang & Luo (2022) proposed the LL-model to quantify the interface coupling between the two interfaces. The equations governing the growth of infinitesimal disturbances at the interfaces as the boundaries of the layer are

$$\nabla^2\phi = 0, \tag{A10}$$

where ϕ is the velocity potential of the fluid, and the kinematic and pressure conditions at the interfaces are

$$\frac{\partial\eta}{\partial t} - \frac{\partial\phi}{\partial y} = 0, \tag{A11}$$

https://doi.org/10.1017/jfm.2025.10281 Published online by Cambridge University Press

$$\rho\frac{\partial\phi}{\partial t}-\rho g\eta+p=p_0. \tag{A12}$$

Here, p is the pressure, g is the acceleration, η is the perturbation shape and p_0 is a constant, which equals the pressure at the interface in the rest state. The system contains two successive interfaces with perturbations η_1 and η_2 separating fluids of densities ρ_1, ρ_2 and ρ_3, and velocity potentials ϕ_1, ϕ_2 and ϕ_3, as sketched in figure 13. The periodic perturbations set at the interfaces are of the form

$$\begin{cases}\eta_1=a_1(t)\cos(kx),\\ \eta_2=a_2(t)\cos(kx),\end{cases} \tag{A13}$$

where $a_1(t)$ and $a_2(t)$ are the amplitudes of the first interface and the second interface, respectively. The following velocity potentials are required in the three fluids:

$$\begin{cases}\phi_1=b_1(t)e^{-k(y-W/2)}\cos(kx),\\ \phi_2=-\left[\dfrac{b_1+b_2}{2}\dfrac{\sinh(ky)}{\cosh(kW/2)}+\dfrac{b_1-b_2}{2}\dfrac{\cosh(ky)}{\sinh(kW/2)}\right]\cos(kx),\\ \phi_3=-b_2(t)e^{k(y+W/2)}\cos(kx),\end{cases} \tag{A14}$$

where b_1 and b_2 are the functions of time in the velocity potentials. Substituting (A13) and (A14) into (A10)–(A12), a pair of ordinary differential equations, i.e. the LL-model (Liang & Luo 2022), is yielded for a_1 and a_2,

$$\begin{cases}\dfrac{\mathrm{d}^2a_1}{\mathrm{d}t^2}[\rho_1+\rho_2\tanh(kW/2)]+\dfrac{\mathrm{d}^2a_2}{\mathrm{d}t^2}[\rho_3+\rho_2\tanh(kW/2)]=kg[(\rho_2-\rho_1)a_1\\ \quad+(\rho_3-\rho_2)a_2],\\ \dfrac{\mathrm{d}^2a_1}{\mathrm{d}t^2}[\rho_1+\rho_2\coth(kW/2)]-\dfrac{\mathrm{d}^2a_2}{\mathrm{d}t^2}[\rho_3+\rho_2\coth(kW/2)]=kg[(\rho_2-\rho_1)a_1\\ \quad-(\rho_3-\rho_2)a_2],\end{cases} \tag{A15}$$

In the previous work (Liang & Luo 2022, 2023*a*), the accelerations g of two successive interfaces were considered the same to quantify the interface coupling. However, as mentioned in our previous work (Chen *et al.* 2024*b*), the accelerations of the two interfaces are different and thus g_1 and g_2 are used to represent the different accelerations of the first and second interfaces, respectively. Based on g_1 and g_2, (A13) and (A14) are substituted into (A10)–(A12) again, and then the LL-model can be rewritten as

$$\begin{cases}\dfrac{\mathrm{d}^2a_1}{\mathrm{d}t^2}[\rho_1+\rho_2\tanh(kW/2)]+\dfrac{\mathrm{d}^2a_2}{\mathrm{d}t^2}[\rho_3+\rho_2\tanh(kW/2)]\\ =k[(\rho_2-\rho_1)a_1g_1+(\rho_3-\rho_2)a_2g_2],\\ \dfrac{\mathrm{d}^2a_1}{\mathrm{d}t^2}[\rho_1+\rho_2\coth(kW/2)]-\dfrac{\mathrm{d}^2a_2}{\mathrm{d}t^2}[\rho_3+\rho_2\coth(kW/2)]\\ =k[(\rho_2-\rho_1)a_1g_1-(\rho_3-\rho_2)a_2g_2].\end{cases} \tag{A16}$$

For UI that has already been accelerated by the RW_1 and DI that has been impacted by the RW_2, as shown in figures 2(*a*)–2(*d*), there are four acceleration processes needed to be considered: the jump velocities of UI induced by TS and the RW_1 (Δu_1 and Δu_{R1}),

https://doi.org/10.1017/jfm.2025.10281 Published online by Cambridge University Press

and the jump velocity of DI induced by TS_1 and the RW_2 (Δu_2 and Δu_{R2}). Due to the very short duration of the waves interacting with the interfaces, the Dirac δ-function is generally used to model the shock interacting with a gas layer (Jacobs *et al.* 1995; Liang & Luo 2023*a*; Chen *et al.* 2024*b*). Accordingly, the accelerations g_1 and g_2 can be expressed as

$$\begin{cases} g_1 = \Delta u_1 \delta(t + t_0) + \Delta u_{R1} \delta(t - t_1), \\ g_2 = \Delta u_2 \delta t + \Delta u_{R2} \delta(t - t_2), \end{cases} \tag{A17}$$

where $t_0 = W_0 / v_1^{TS}$ is the time difference between TS accelerating UI and TS_1 impacting DI. Substituting (A17) into (A16) and integrating the equations, a new model for predicting the linear growth rates of the perturbations at UI hit by the RW_1 ($\dot{a}_{11}$) and DI stretched by the RW_2 ($\dot{a}_{21}$) is established

$$\begin{aligned} &\dot{a}_{11}[\rho_1 + \rho_2 \tanh(kW/2)] + \dot{a}_{21}[\rho_3 + \rho_2 \tanh(kW/2)] \\ &\quad = k(\rho_2 - \rho_1)(a_{1+}\Delta u_1 + a_{1R}^{+}\Delta u_{R1}) + k(\rho_3 - \rho_2)(a_{20}\Delta u_2 + a_{2R}^{+}\Delta u_{R2}), \end{aligned} \tag{A18}$$

$$\begin{aligned} &\dot{a}_{11}[\rho_1 + \rho_2 \coth(kW/2)] - \dot{a}_{21}[\rho_3 + \rho_2 \coth(kW/2)] \\ &\quad = k(\rho_2 - \rho_1)(a_{1+}\Delta u_1 + a_{1R}^{+}\Delta u_{R1}) - k(\rho_3 - \rho_2)(a_{20}\Delta u_2 + a_{2R}^{+}\Delta u_{R2}). \end{aligned} \tag{A19}$$

Equations (A18) and (A19), i.e. (2.1) and (2.2) in § 2, constitute the modified LL-model. According to the impulsive model (Richtmyer 1960) and the MB model (Meyer & Blewett 1972), a_{1+} is the amplitude of UI just after being impacted by TS and $a_{20} = (a_{2-} + a_{2+})/2$ is the average amplitude of the shocked and unshocked DI in (A18)–(A19). The parameters a_{1R}^{+} and a_{2R}^{+}, which have been expressed in (A4) and (A9), are the amplitudes of UI just being accelerated by the RW_1 and of DI just being impacted by the RW_2, respectively. Here, for the shocked system, ρ_1, ρ_2 and ρ_3 are calculated as the densities of fluid 1, fluid 2 and fluid 3, respectively, after the interaction of the RW_2 with DI; W is the distance between UI and DI after TS_1 collides with DI, and can be expressed as $W = W_0(1 - \Delta u_1 / v_1^{TS})$.

After RW_2 interact with DI, the two compression waves (CW_1 and CW_2) reflected from AI move downstream and impact UI and DI, as shown in figures 2(*e*)–2(*f*). As discussed in § 2, based on the modified-LL model, the perturbation growth rates at UI and DI induced by CW_1, CW_2 and the subsequent reverberating waves can be calculated by

$$\begin{aligned} &\dot{a}_{1C}[\rho_{1C} + \rho_{2C} \tanh(kW_C/2)] + \dot{a}_{2C}[\rho_{3C} + \rho_{2C} \tanh(kW_C/2)] \\ &\quad = k(\rho_{2C} - \rho_{1C})a_{1C}\Delta u_{1C} + k(\rho_{3C} - \rho_{2C})a_{2C}\Delta u_{2C}, \end{aligned} \tag{A20}$$

$$\begin{aligned} &\dot{a}_{1C}[\rho_{1C} + \rho_{2C} \coth(kW_C/2)] - \dot{a}_{2C}[\rho_{3C} + \rho_{2C} \coth(kW_C/2)] \\ &\quad = k(\rho_{2C} - \rho_{1C})a_{1C}\Delta u_{1C} - k(\rho_{3C} - \rho_{2C})a_{2C}\Delta u_{2C}. \end{aligned} \tag{A21}$$

Here, Δu_{1C} and Δu_{2C} are the sum of jump velocities of UI and DI accelerated by the reverberating waves in figures 2(*f*)–2(*j*), respectively; ρ_{1C}, ρ_{2C} and ρ_{3C} are the densities of fluid 1, fluid 2 and fluid 3 after the RW_8 interact with DI; W_C is the distance between UI and DI after the CW_1 accelerate DI, calculated as $W_C = W[1 + (\Delta u_2 - \Delta u_1)/c_1][1 + (\Delta u_2 - \Delta u_1 - \Delta u_{R1})/c_2][1 - (u_{C1} - \Delta u_2 - \Delta u_{R2})/c_4]$, where u_{C1} is the velocity of UI after being impacted by the CW_1 and c_4 is the sound speed of the fluid 2 after the RW_2

https://doi.org/10.1017/jfm.2025.10281 Published online by Cambridge University Press

passes through DI. After defining t_{C1} and t_{C2} as the times of UI and DI being accelerated by CW_1, respectively, the amplitudes of UI and DI just prior to the CW_1 acceleration can be obtained as

$$\begin{cases} a_{1C} = a_{1R}^{+} + \dot{a}_{11}(t_{C1} - t_1), \\ a_{2C} = a_{2R}^{+} + \dot{a}_{21}(t_{C2} - t_2). \end{cases} \tag{A22}$$

According to (A1)–(A22), (2.5) can be theoretically calculated.

Appendix B. Effect of UI amplitude on the perturbation growth at DI

While prior cases in this work assume an unperturbed upstream UI, the influence of UI amplitude on the perturbation evolution of the downstream DI remains unexamined. To address this gap, we conduct two additional numerical simulations with initial scaled UI amplitudes $ka_{1-} = 0.1$ and $ka_{1-} = -0.1$, probing their role in modulating amplitude evolution at DI. These cases retain the DI's initial scaled amplitude $ka_{2-} = 0.1$ (identical to previous configurations) and replicate all other parameters from case 10-57.2, where DI amplitude stagnation was observed. A comparative analysis of amplitude evolution across perturbed UI cases and the baseline (case 10-57.2) is presented in figure 14.

Theoretically, the shocked UI amplitude $a_{1+} = a_{1-}(1 - \Delta u_1 / v_0^{TS})$, where v_0^{TS} is the TS velocity, and the amplitude TS_1 is derived by the model proposed by Ishizaki & Nishihara (1997). By integrating models in Appendix A, we can predict the amplitude evolution of UI and DI when UI is initially perturbed. These theoretical predictions, represented by solid lines in figure 14, are validated against numerical results, denoted by symbols. Figure 14(*a*) reveals that, prior to the compression waves' arrival, the UI amplitude growth is amplified for perturbed cases ($ka_{1-} = \pm 0.1$) compared with the unperturbed baseline ($ka_{1-} = 0$). Notably, for $ka_{1-} = 0.1$ ($ka_{1-} = -0.1$), the amplitude evolves into the negative (positive) phase, which is similar to the behaviour of a shocked single UI. After the compression waves interact with DI, the UI growth reverses direction in all cases, with theoretical predictions aligning closely with numerical simulations.

As shown in figure 14(*b*), prior to the compression waves' interaction, the DI amplitude grows negatively at comparable rate across all ka_{1-} cases. After compression waves interact with DI, however, the DI's evolution diverges. For $ka_{1-} = 0.1$, the amplitude

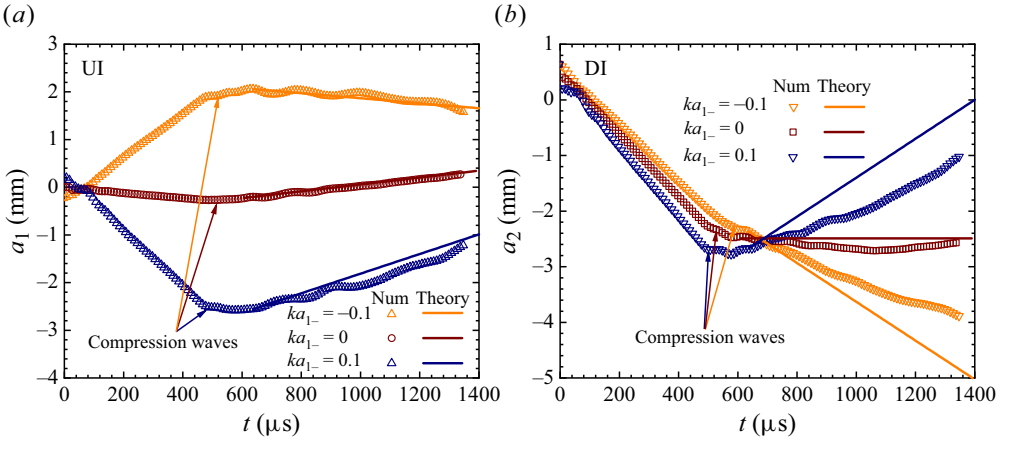


Figure 14. Comparison of the amplitudes of UI (*a*) and DI (*b*) obtained from the cases with $ka_{1-} = -0.1$, $ka_{1-} = 0$ and $ka_{1-} = 0.1$. Symbols (lines) represent numerical (theoretical) results.

https://doi.org/10.1017/jfm.2025.10281 Published online by Cambridge University Press

reverses direction, while for $ka_{1-} = -0.1$, growth persists in the negative direction but at a diminished rate. From figures 14(*a*) and 14(*b*), after compression waves perturb both interfaces, UI and DI amplitudes evolve synchronously in the same direction. This coupling suggests that initial UI perturbations significantly influence the DI's evolution, potentially disrupting the amplitude 'freeze out' achievable with an initially flat UI. While theoretical predictions align with the UI evolution, discrepancies arise for DI when $ka_{1-} = \pm 0.1$. These deviations likely stem from the model's current omission of disturbed gas flow effects behind the perturbed transmitted shock on DI evolution, a mechanism requiring further investigation.

References

ABGRALL, R. & KARNI, S. 2001 Computations of compressible multifluids. *J. Comput. Phys.* **169** (2), 594–623.

AMENDT, P. 2021 Entropy generation from hydrodynamic mixing in inertial confinement fusion indirect-drive targets. *Phys. Plasmas* **28** (7), 072701.

BETTI, R. & HURRICANE, O.A. 2016 Inertial-confinement fusion with lasers. *Nat. Phys.* **12** (5), 435–448.

BILLET, G. & ABGRALL, R. 2003 An adaptive shock-capturing algorithm for solving unsteady reactive flows. *Comput. Fluids* **32** (10), 1473–1495.

BODNER, S.E. *et al.* 1998 Direct-drive laser fusion: status and prospects. *Phys. Plasmas* **5** (5), 1901–1918.

BROUILLETTE, M. 2002 The Richtmyer–Meshkov instability. *Annu. Rev. Fluid Mech.* **34** (1), 445–468.

CAO, Q., LI, J., WANG, H., ZHAI, Z. & LUO, X. 2024 Coupled Richtmyer–Meshkov and Kelvin–Helmholtz instability on a shock-accelerated inclined single-mode interface. *J. Fluid Mech.* **996**, A37.

CHARAKHCH'YAN, A.A. 2000 Richtmyer–Meshkov instability of an interface between two media due to passage of two successive shocks. *J. Appl. Mech. Tech. Phys.* **41** (1), 23–31.

CHARAKHCH'YAN, A.A. 2001 Reshocking at the non-linear stage of Richtmyer–Meshkov instability. *Plasma Phys. Control. Fusion* **43** (9), 1169–1179.

CHEN, C., LI, J., WANG, H., ZHAI, Z. & LUO, X. 2025 Attenuation of Richtmyer–Meshkov instability growth of fluid layer via double shock. *Sci. China-Phys. Mech. Astron.* **68** (4), 244711.

CHEN, C., LI, J., ZHAI, Z. & LUO, X. 2024*a* Effects of disturbed transmitted shock and interface coupling on heavy gas layer evolution. *Phys. Fluids* **36** (8), 086108.

CHEN, C., WANG, H., ZHAI, Z. & LUO, X. 2023*a* Attenuation of perturbation growth of single-mode sf_6-air interface through reflected rarefaction waves. *J. Fluid Mech.* **969**, R1.

CHEN, C., WANG, H., ZHAI, Z. & LUO, X. 2024*b* Mode coupling between two different interfaces of a gas layer subject to a shock. *J. Fluid Mech.* **984**, A38.

CHEN, C., XING, Y., WANG, H., ZHAI, Z. & LUO, X. 2023b Freeze-out of perturbation growth of single-mode helium–air interface through reflected shock in Richtmyer–Meshkov flows. *J. Fluid Mech.* **956**, R2.

CONG, Z., GUO, X., ZHOU, Z., CHENG, W. & SI, T. 2024 Freeze-out of perturbation growth for shocked heavy fluid layers by eliminating reverberating waves. *J. Fluid Mech.* **987**, A10.

DIMONTE, G. & RAMAPRABHU, P. 2010 Simulations and model of the nonlinear Richtmyer–Meshkov instability. *Phys. Fluids* **22** (1), 014104.

DING, J., SI, T., CHEN, M., ZHAI, Z., LU, X. & LUO, X. 2017 On the interaction of a planar shock with a three-dimensional light gas cylinder. *J. Fluid Mech.* **828**, 289–317.

ISHIZAKI, R. & NISHIHARA, K. 1997 Propagation of a rippled shock wave driven by nonuniform laser ablation. *Phys. Rev. Lett.* **78** (10), 1920–1923.

JACOBS, J.W., JENKINS, D.G., KLEIN, D.L. & BENJAMIN, R.F. 1995 Nonlinear growth of the shock-accelerated instability of a thin fluid layer. *J. Fluid Mech.* **295** (−1), 23–42.

JACOBS, J.W., KLEIN, D.L., JENKINS, D.G. & BENJAMIN, R.F. 1993 Instability growth patterns of a shock-accelerated thin fluid layer. *Phys. Rev. Lett.* **70** (5), 583–586.

JIANG, G. & SHU, C. 1996 Efficient implementation of weighted ENO schemes. *J. Comput. Phys.* **126** (1), 202–228.

KRITCHER, A.L. *et al.* 2022 Design of inertial fusion implosions reaching the burning plasma regime. *Nat. Phys.* **18** (3), 251–258.

KURANZ, C. *et al.* 2018 How high energy fluxes may affect Rayleigh–Taylor instability growth in young supernova remnants. *Nat. Commun.* **9** (1), 1564.

LI, J., CAO, Q., WANG, H., ZHAI, Z. & LUO, X. 2023 New interface formation method for shock-interface interaction studies. *Exp. Fluids* **64** (11), 170.

https://doi.org/10.1017/jfm.2025.10281 Published online by Cambridge University Press

LI, J., CHEN, C., ZHAI, Z. & LUO, X. 2024 Effects of compressibility on Richtmyer–Meshkov instability of heavy/light interface. *Phys. Fluids* **36** (5), 056104.
LIANG, Y. 2022 The phase effect on the Richtmyer–Meshkov instability of a fluid layer. *Phys. Fluids* **34** (3), 034106.
LIANG, Y. & LUO, X. 2021 Shock-induced dual-layer evolution. *J. Fluid Mech.* **929**, R3.
LIANG, Y. & LUO, X. 2022 On shock-induced evolution of a gas layer with two fast/slow interfaces. *J. Fluid Mech.* **939**, A16.
LIANG, Y. & LUO, X. 2023*a* Hydrodynamic instabilities of two successive slow/fast interfaces induced by a weak shock. *J. Fluid Mech.* **955**, A40.
LIANG, Y. & LUO, X. 2023*b* Review on hydrodynamic instabilities of a shocked gas layer. *Sci. China-Phys. Mech. Astron.* **66** (10), 104701.
LIU, L., LIANG, Y., DING, J., LIU, N. & LUO, X. 2018*a* An elaborate experiment on the single-mode Richtmyer–Meshkov instability. *J. Fluid Mech.* **853**, R2.
LIU, W., LI, X., YU, C., FU, Y., WANG, P., WANG, L. & YE, W. 2018*b* Theoretical study on finite-thickness effect on harmonics in Richtmyer-Meshkov instability for arbitrary Atwood numbers. *Phys. Plasmas* **25** (12), 122103.
LOBATCHEV, V. & BETTI, R. 2000 Ablative stabilization of the deceleration phase Rayleigh–Taylor instability. *Phys. Rev. Lett.* **85** (21), 4522–4525.
MERRITT, E.C. *et al.* 2023 Same-sided successive-shock HED instability experiments. *Phys. Plasmas* **30** (7), 072108.
MESHKOV, E.E. 1969 Instability of the interface of two gases accelerated by a shock wave. *Fluid Dyn.* **4** (5), 101–104.
MEYER, K.A. & BLEWETT, P.J. 1972 Numerical investigation of the stability of a shock-accelerated interface between two fluids. *Phys. Fluids* **15** (5), 753–759.
MIKAELIAN, K.O. 2010 Analytic approach to nonlinear hydrodynamic instabilities driven by time-dependent accelerations. *Phys. Rev. E* **81** (1), 016325.
MIKAELIAN, K.O. 1985 Richtmyer–Meshkov instabilities in stratified fluids. *Phys. Rev. A* **31** (1), 410–419.
MIKAELIAN, K.O. 1996 Numerical simulations of Richtmyer–Meshkov instabilities in finite-thickness fluid layers. *Phys. Fluids* **8** (5), 1269–1292.
MIKAELIAN, K.O. 2025 Feedthrough and suppression of Rayleigh–Taylor and Richtmyer–Meshkov instabilities. *Phys. Fluids* **37** (3), 032114.
QIAO, X. & LAN, K. 2021 Novel target designs to mitigate hydrodynamic instabilities growth in inertial confinement fusion. *Phys. Rev. Lett.* **126** (18), 185001.
RANJAN, D., OAKLEY, J. & BONAZZA, R. 2011 Shock-bubble interactions. *Annu. Rev. Fluid Mech.* **43** (1), 117–140.
RICHTMYER, R.D. 1960 Taylor instability in shock acceleration of compressible fluids. *Commun. Pure Appl. Maths* **13** (2), 297–319.
SCHALLES, M., LOUIE, C., PEABODY, K., SADLER, J., ZHOU, Y. & JACOBS, J. 2024 Shock tube experiments on the three-layer Richtmyer–Meshkov instability. *Phys. Fluids* **36** (1), 014126.
SCHILL, W.J. *et al.* 2024 Suppression of Richtmyer-Meshkov instability via special pairs of shocks and phase transitions. *Phys. Rev. Lett.* **132** (2), 024001.
SPEARS, B.K. *et al.* 2014 Mode 1 drive asymmetry in inertial confinement fusion implosions on the national ignition facility. *Phys. Plasmas* **21** (4), 042702.
STERBENTZ, D.M., JEKEL, C.F., WHITE, D.A., AUBRY, S., LORENZANA, H.E. & BELOF, J.L. 2022 Design optimization for Richtmyer–Meshkov instability suppression at shock-compressed material interfaces. *Phys. Fluids* **34** (8), 082109.
URZAY, J. 2018 Supersonic combustion in air-breathing propulsion systems for hypersonic flight. *Annu. Rev. Fluid Mech.* **50** (1), 593–627.
VANDENBOOMGAERDE, M., MÜGLER, C. & GAUTHIER, S. 1998 Impulsive model for the Richtmyer–Meshkov instability. *Phys. Rev. E* **58** (2), 1874–1882.
VELIKOVICH, A. & PHILLIPS, L. 1996 Instability of a plane centered rarefaction wave. *Phys. Fluids* **8** (4), 1107–1118.
WEST, S.R., SADLER, J.D., POWELL, P.D. & ZHOU, Y. 2024 Shock-driven three-fluid mixing with various chevron interface configurations. *Phys. Fluids* **36** (10), 104132.
ZHAI, Z., CHEN, C., XING, Y., LI, J., CAO, Q., WANG, H. & LUO, X. 2025 Manipulation of Richtmyer–Meshkov instability on a heavy–light interface via successive shocks. *J. Fluid Mech.* **1003**, A9.
ZHOU, Y. 2017a Rayleigh–Taylor and Richtmyer–Meshkov instability induced flow, turbulence, and mixing. I. *Phys. Rep.* **720-722**, 1–136.

https://doi.org/10.1017/jfm.2025.10281 Published online by Cambridge University Press

ZHOU, Y. 2017*b* Rayleigh–Taylor and Richtmyer–Meshkov instability induced flow, turbulence, and mixing. II. *Phys. Rep.* **723-725**, 1–160.

ZHOU, Y., SADLER, J.D. & HURRICANE, O.A. 2025 Instabilities and mixing in inertial confinement fusion. *Annu. Rev. Fluid Mech.* **57** (1), 197–225.

ZHOU, Y. *et al.* 2021 Rayleigh–Taylor and Richtmyer–Meshkov instabilities: A journey through scales. *Physica D* **423**, 132838.

ZYLSTRA, A.B. *et al.* 2022 Burning plasma achieved in inertial fusion. *Nature* **601** (7894), 542–548.

https://doi.org/10.1017/jfm.2025.10281 Published online by Cambridge University Press